Research Article

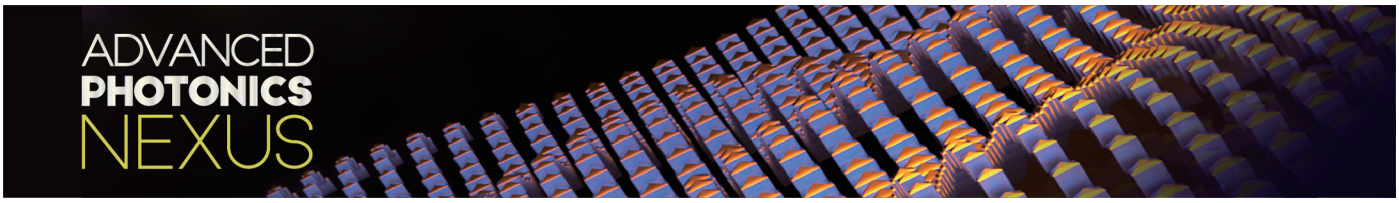

Intelligent soliton molecules control in an ultrafast thulium fiber laser

Yi Zhou,[a,*] Kangwen Yang,[a,b,c] Kevin K. Tsia,[a,b] Heping Zeng,[d] and Kenneth K. Y. Wong[a,b,*]
[a]The University of Hong Kong, Department of Electrical and Electronic Engineering, Hong Kong, China
[b]Advanced Biomedical Instrumentation Centre, New Territories, Hong Kong, China
[c]University of Shanghai for Science and Technology, Ministry of Education, School of Optical Electrical and Computer Engineering, Shanghai Key Laboratory of Modern Optical System, and Engineering Research Center of Optical Instrument and System, Shanghai, China
[d]East China Normal University, State Key Laboratory of Precision Spectroscopy, Shanghai, China

Abstract. Soliton molecules (SMs), bounded and self-assembled of particle-like dissipative solitons, exist with versatile mutual interactions and manifest substantial potential in soliton communication and optical data storage. However, controllable manipulation of the bounded molecular patterns remains challenging, as reaching a specific operation regime in lasers generally involves adjusting multiple control parameters in connection with a wide range of accessible pulse dynamics. An evolutionary algorithm is implemented for intelligent control of SMs in a 2 μm ultrafast fiber laser mode locked through nonlinear polarization rotation. Depending on the specifications of the merit function used for the optimization procedure, various SM operations are obtained, including spectra shape programming and controllable deterministic switching of doublet and triplet SMs operating in stationary or pulsation states with reconfigurable temporal separations, frequency locking of pulsation SMs, doublet and SM complexes with controllable pulsation ratio, etc. Digital encoding is further demonstrated in this platform by employing the self-assembled characteristics of SMs. Our work opens up an avenue for active SM control beyond conventional telecom bands and brings useful insights into nonlinear science and applications.

Keywords: mode locking; optical soliton molecule; ultrafast fiber lasers.

Received Dec. 9, 2024; accepted for publication Jan. 2, 2025; published online Jan. 21, 2025.

[DOI: 10.1117/1.APN.4.1.016012]

1 Introduction

Ultrafast pulses delivered from mode-locked fiber lasers stimulate extensive applications in industry and ultrafast science.[1–7] In addition, mode-locked fibers constitute an ideal platform for the fundamental exploration of complex nonlinear wave dynamics. In particular, such lasers are based on the nonlinear polarization rotation (NPR) mechanism to drive the mode locking. The high levels of linear and nonlinear effects accumulated during the intracavity evolution entail a wealth of complex ultrashort pulse dynamics that can be accessed by tuning the cavity parameters.[8–13] More than the elementary pulse entity, termed dissipative soliton, originating from the interplays between dispersion/nonlinearity and gain/loss,[14,15] these short pulses can also self-assembled and bounded to form soliton molecules (SMs), endowed by the balanced interaction forces.[16–20] Similar to matter molecules, many unveiled internal motions in SMs emphasize the light–matter analogy. Such self-organized patterns, including soliton pair molecules, soliton molecular complexes (SMCs), and supramolecular structures,[21–25] display plentiful internal dynamics in the presence of energy exchange between each constituent, as well as being attractive in applications of increasing telecommunication capacity and all-optical information storage.[6]

Recently, the use of time-stretch dispersion Fourier transform (TS-DFT) techniques,[26] a spectral-to-temporal mapping method enabling real-time spectra acquisition, has further facilitated the direct observation of inherent nonlinear evolutionary dynamics related to the generation and evolution of SMs. These long-lasting studies on the transient SM dynamics also raise the question of how far the "molecular" analogy reaches, that is, whether diverse dimensions of SMs can be controllably driven

*Address all correspondence to Yi Zhou, zhouyi08@hku.hk; Kenneth K. Y. Wong, kywong@eee.hku.hk

or manipulated, including intersoliton temporal separation, relative intensity and phase, and stationary or oscillating operation. In consideration of the energy exchange within molecular structures, direct pump modulation can be exploited to achieve SMs fast switching between discrete bounded states, mainly referring to the temporal separation or relative phase.[27–31] In parallel, on-demand harnessing of SMs between different temporal separations can be achieved by varying the group-velocity dispersion and dispersion loss.[32] However, comprehensive and precise manipulation of the multiple properties of SMs (intersoliton separation, stationary or pulsation operation, frequency locking, and tunable pulsation ratio) in a real-time manner remains a challenge and has been largely unexplored in experiments. Moreover, reaching a desired operating regime of SMs in lasers generally depends on precisely adjusting multiple parameters in a high-dimension space, which often requires a lengthy, trial-and-error experimental procedure. Due to the lack of analytic relationship between cavity parameters and specific soliton operations, the problem of repeatability also hampers the possibility of obtaining an augmented subspace of desired SM states through tuning intracavity parameters.

Despite this, the use of machine-learning strategies or evolutionary algorithms can circumvent such difficulties. Utilizing advanced algorithmic tools, adaptive feedback, and control systems has recently greatly boosted progress in laser optimization, and numerous approaches have been reported to automate optimization of one or more parameters of the laser cavity to reach and maintain a desired soliton operation state.[33–41] The ongoing discovery of internal molecular dynamics using advanced spectral observation (TS-DFT) can further enrich the manipulation mechanism of SMs. In this work, we implement intelligent SM control by combining an evolution algorithm (EA) and electronic polarization controller (EPC) in a 2 μm NPR mode-locked fiber laser, based on the optimal three-parameter tuning of the intracavity nonlinear transfer function through electronically driven polarization control. The Tm-doped fiber (TDF) laser utilized here possesses a highly desirable broad wavelength range, spanning ~350 nm around 2 μm. Such unique operation bandwidth has placed these fiber laser systems at the forefront of diverse applications, e.g., optical coherence tomography,[42] nonlinear microscopy,[43] and optical communication.[44,45] The larger gain bandwidth and shorter excited-state relaxation time can also provide unique opportunities to explore novel pulse solutions that significantly differ from those of Yb/Er lasers. Here, we define the fitness function of EA relying on the spectral pattern or the features of the radio-frequency (RF) spectrum of the laser output, which is capable of achieving SM control in different dimensions, including spectral shape programming and controllable deterministic switching of doublet and triplet SMs operating in stationary or pulsation states with different intersoliton separation, frequency locking of pulsation SMs, doublet and SMCs with a controllable pulsation ratio. Exemplary digital encoding was further demonstrated in this platform. The proposed intelligent control of SMs opens an emerging window toward longer wavelengths and provides an ideal platform for both diverse applications in optical information technology and research on SM-related laser dynamics.

2 Results and Discussion

2.1 Experimental Setups and Principles

The experimental setup of a Tm-doped mode-locked fiber laser, shown in Fig. 1(a), is meant to generate the SM with different operations. This ring fiber laser is mode-locked based on the NPR mechanism. The nonlinear transfer function of the NPR mode locking is controlled by the EPC and thus is a quasi-instantaneous saturable absorber. The 12 m long ring cavity includes 2.8 m of TDF (TSF-9–125) with group velocity dispersion (GVD) of ~ -83 ps^2/km and 9.2 m SM28-e fiber with a GVD of ~ -71 ps^2/km, which is pumped by the laser source at 1570 nm. The net cavity dispersion is -0.885 ps^2 and corresponds to a fundamental repetition rate of 16.62 MHz. A bandpass spectral filter was inserted into the cavity to fix the optical spectrum with a central wavelength of 1970 nm.

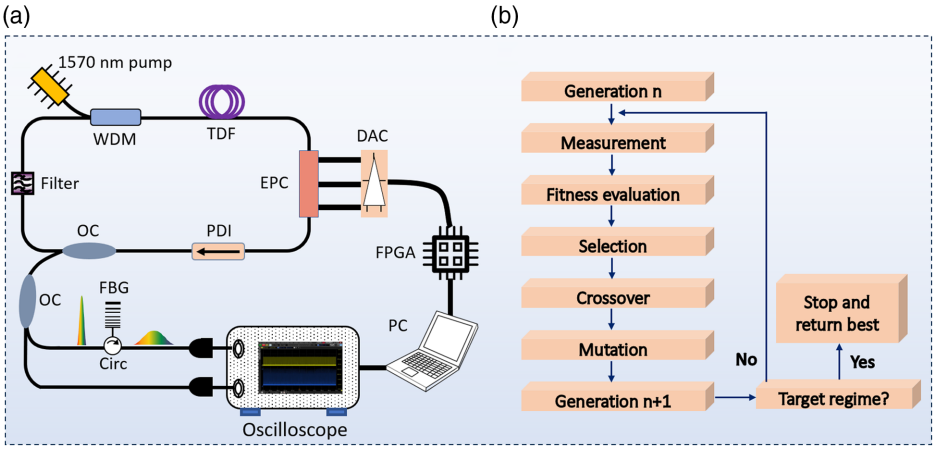

Fig. 1 The experimental configuration. (a) The ultrafast fiber laser setup. Controlling the SMs in the laser can be done in the EPC-based feedback loop. The spectral information is obtained through the OSA or oscilloscope along with TS-DFT, where the FBG is used as the dispersion medium. WDM, wavelength division multiplexing; TDF, thulium-doped fiber; PDI, polarization-dependent isolator; EPC, electronic polarization controller; OC, optical coupler; FBGA, field-programmable gate array; PC, computer; DAC, digital-to-analog converter; FBG, fiber Bragg grating; Circ, circulator. (b) The flow chart of the EA.

A coupler with a 30/70 splitting ratio was used to extract part of the output power for measurements. The pulse optical spectra were measured through an optical spectrum analyzer (OPA, YOKOGAWA, AQ6375), and the undispersed temporal intensity information was detected by a high-speed oscilloscope (Keysight, DSOV204A) with a photodetector (12.5 GHz bandwidth). To investigate the real-time SMs' spectral evolution, a chirped fiber Bragg grating (CFBG) was equipped before another photodetector (12.5 GHz bandwidth) to achieve the wavelength-to-time conversion via the TS-DFT technique. The custom-made CFBG from TeraXion has a linear dispersion of 300 ps/nm and a flat reflection band of 30 nm between 1955 and 1985 nm. The temporal and spectral resolution in this experiment was 80 ps and 0.29 nm, respectively.[46]

As the primary control element for intracavity polarization, the EPC consists of three fiber squeezers oriented at 45 deg to each other, and each fiber squeezer was driven by the digital-to-analog converters (DACs) with a specific voltage signal. The EPC, with a response time of milliseconds, can generate all possible states of polarization over the Poincaré sphere; thereby, only one EPC is required in the laser cavity to achieve complete control of the nonlinear transfer function. In the feedback-loop control, the pulse information acquired by the OSA or oscilloscope is transmitted to a computer, which acts as a core for EA running. The computer then sends commands to the FPGA based on the optimization algorithm results, setting control voltages to drive the EPC through the DACs.

2.2 Spectral Shape Programming of SMs

To achieve the intelligent control of SMs, the design of the EA is critical; it is illustrated in Fig. 1(b). The genetic algorithm (GA) is used here and combines user-defined merit function (fitness or objective function) to achieve the SMs' flexible control. The transformation among different SM states generally only requires a minor perturbation of polarization or pump power. The fitness of intersoliton separation represents the temporal interval between multiple solitons in SMs, determined by the optical spectral modulation period. The solitons' temporal separation, soliton number, and stationary or pulsation state in SMs correspond to particular spectral shapes recorded through OSA or TS-DFT. These features of SMs can also be reflected in the field autocorrelation traces, e.g., the peak number (main peak and side peaks), peak intensity oscillation, and temporal location of side peaks. Note that the field autocorrelation traces are calculated based on the measured spectra through a fast Fourier transform, thereby remaining determined by the specific spectral shapes of SMs as one of the vital fitness functions.

In this experiment, the OSA or TS-DFT captures the pulses' spectral information, and different objective spectra correspond to different SM states. Thus, a set of experimental data (spectral waveform) corresponding to the objective spectral shape is required to acquire the standard pulses. The fitness function in spectral shape programming is the normalized mean square error (NMSE) between the current and standard spectra. A threshold is set as the upper limit of the NMSE. When the NMSE is lower than a preset threshold, the objective spectral shape is successfully fitted, and the EA will stop the searching procedure.

A doublet SM in the experiment can be generated with an output power of 6.55 mW when turning the pump power to 420 mW. Figures 2(a) and 2(b) show the spectral shape programming results of doublet SMs and compare the acquired spectra after fitting with the standard spectra, suggesting an NMSE of only 0.0051 and 0.0010, a nearly perfect fit. For various spectral shapes, the NMSE reveals the discrepancy between the current and standard pulses. According to the experiment, empirically, an NMSE lower than ∼0.01 usually represents a good fit. The acquired two spectra [Figs. 2(a) and 2(d)] with different interference fringe modulation periods indicate the SMs with distinct temporal separation, which is further verified by the DFT spectra and field autocorrelation trace of two SM states, as shown in Figs. 2(b), 2(c), 2(e), and 2(f) [corresponding to the dashed rectangle in Fig. 2(g)]. One of the SMs represents a weak pulsation state and a smaller intersoliton temporal separation [Figs. 2(b) and 2(c)], which is consistent with the spectrum feature [Fig. 2(a)]. Another SM signifies a stationary operation and larger temporal interval [Figs. 2(e) and 2(f)]. After successfully acquiring the desired spectrum with EA optimization, the deterministic switching of SMs can be achieved by simply changing the drive voltage of EPC, as shown in Figs. 2(g) and 2(h). The doublet SM switches from pulsation to a stationary state with an increase in the intersoliton temporal separation.

Similarly, the triplet SM can be generated in the fiber laser with an output power of 7.6 mW when slightly increasing the pump power to 440 mW. The spectral shape programming results of triplet SMs are shown in Figs. 2(i) and 2(l). A comparison between the acquired and standard spectra suggests the NMSE of 0.0005 and 0.0042, demonstrating a good fit. The different spectral modulation periods [Figs. 2(i) and 2(l)] indicate the distinct intersoliton separation of two triplet SM states and are further verified by the field autocorrelation traces [Figs. 2(k) and 2(n)]. The corresponding DFT spectral evolution [Figs. 2(j) and 2(m)] exhibit the two triplet SM states with moderate pulsation behavior, further verified by the single-shot spectral variation in one pulsation period (see Fig. S1 in the Supplementary Material). Like the doublet SM, the deterministic switching of the triplet SM can be achieved by changing the optimized drive voltage of EPC [Figs. 2(o) and 2(p)]. The pulsation triplet SM switches with different spectral features and a decrease in the intersoliton temporal separation. The inset in Figs. 2(h) and 2(p) further reflects the solitons' temporal distribution in SMs during switching, which is consistent with the specific spectral characteristics. Moreover, the output power of pulses with the increased pump power, the internal motion (the relative phases and temporal separations among solitons) of doublet and triplet SMs during switching, as well as numerical simulation of SMs switching, can be found in Figs. S2–S6 in the Supplementary Material.

2.3 Evolutionary Algorithm Optimization of Pulsation SMs

In addition to the extensively explored stationary SMs, pulsation SMs with pronounced spectral variation in one pulsation period can also be generated in the laser depending on adjusting the intracavity polarization precisely, which can be efficiently searched through the EA. Here, we introduced an approach based on the EA to search and control an SM pulsation state in the fiber laser. The fitness functions rely on detecting and controlling the crucial parameters of pulsation operation and pulsation frequency to tune the pulsation ratio and achieve pulsation frequency locking of SMs. During the search process, the operation state of SMs is characterized in real time via the

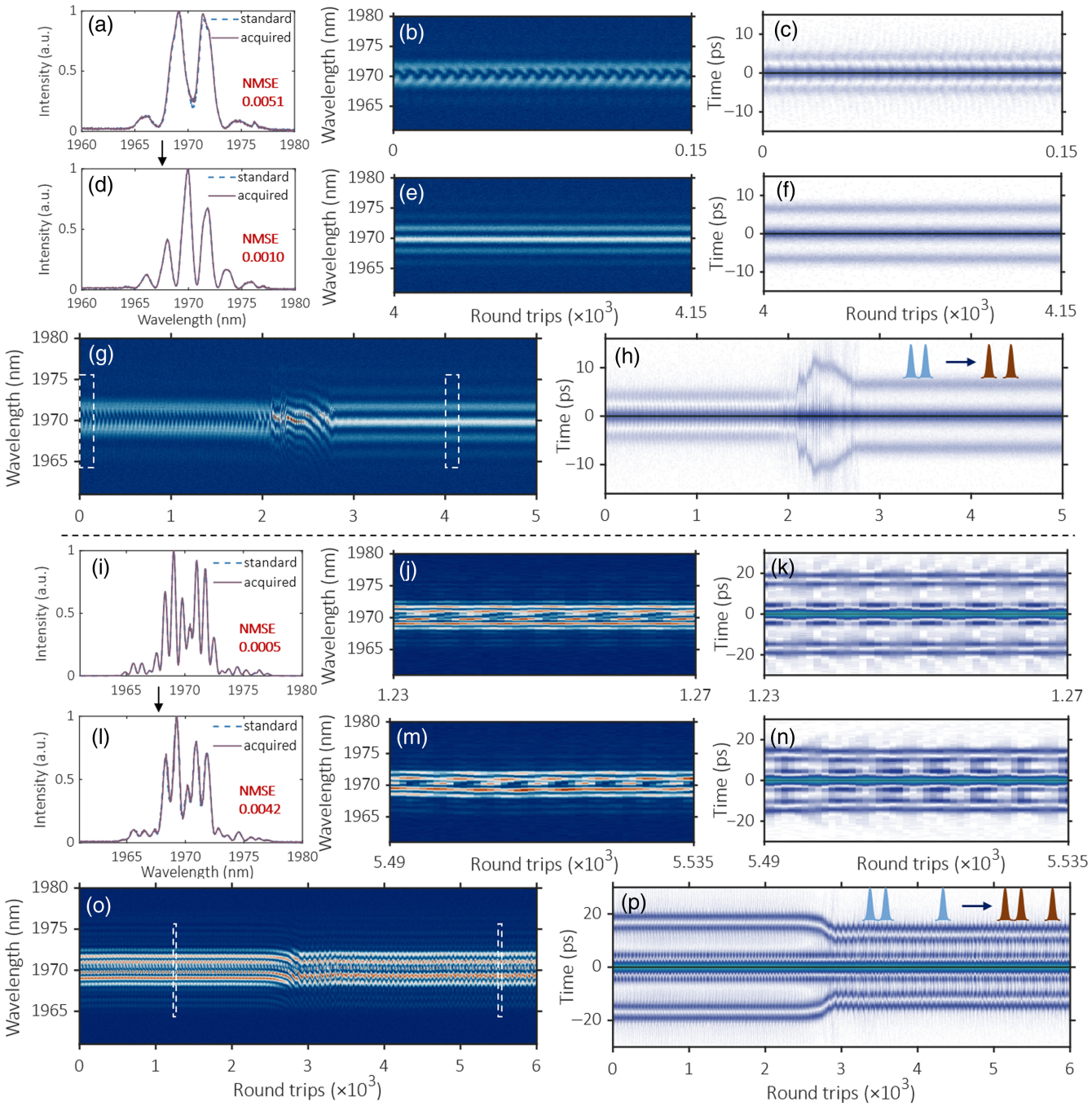

Fig. 2 Spectral shape programming of SMs. (a)–(h) Spectrum programming results of doublet SM. (a), (d) Acquired and standard doublet SM spectrum with NMSE of 0.0051 and 0.0010, respectively. (b), (e) DFT spectra and (c), (f) field autocorrelation trace evolution over consecutive RTs corresponding to (a) and (d), respectively. (g) DFT spectra and (h) field autocorrelation trace evolution of doublet SM deterministic switching (a)–(d). (i)–(p) Spectrum programming results of triplet SM. (i), (l) Acquired and standard triplet SM spectrum with NMSE of 0.0005 and 0.0042, respectively. (j), (m) DFT spectra and (k), (n) field autocorrelation trace evolution over consecutive RTs corresponding to (i) and (l), respectively. (o) DFT spectra and (p) field autocorrelation trace evolution of triplet SM deterministic switching (i)–(l).

oscilloscope and TS-DFT technique, which is linked to a computer running the EA and cpntro;s the intracavity polarization through the EPC via a driver to lock the SMs to the desired pulsation regime [Figs. 1(a) and 1(b)]. Here, we develop an approach simply to achieve the pulsation frequency locking of SMs so that EA tunes the SMs to these desired states. The defined merit function is modified compared to Ref. 40, and considering the trait of the frequency-locking operation,[47,48] namely, maximizes the SNR of the pulsation frequency [Fig. 3(a)]. The modified merit function is given in the Methods section.

Here, the fitness in the tuning stage is the pulsation frequency manifests as a sideband in the RF spectrum, as illustrated in Fig. 3(a), where $|f_{\pm 1} - f_r|$ represents the pulsation frequency, and f_r and $f_{\pm 1}$ are the cavity repetition rate and sideband frequency, respectively.

Figure 3(b) depicts the evolution of the maximum merit scores of the population over successive generations. The fitness value grows rapidly and converges to a maximum value after nine generations, thus indicating the generation of pulsation SMs along with the frequency-locked operation mode. Figures 3(e) and 3(f) show the corresponding DFT spectra- and field-autocorrelated trace evolution with EA optimization. In contrast to the stationary SM, the DFT spectra of the pulsation SM show periodic variation in spectral shape and amplitude, which is a salient feature of pulsation SM. In contrast, another pulsation SM can be generated in the laser by tuning intracavity polarization without EA optimization [Figs. 3(g) and 3(h)]. The DFT spectra and field autocorrelation trace evolution indicate that the quality of the periodic behavior is clearly degraded in comparison to Figs. 3(e) and 3(f). Further, the RF spectra, obtained by the Fourier transform, and the DFT signal from the photodiode reveal the major difference between the two types of pulsation SMs. The pulsation frequency of the unstable SM state [Fig. 3(g)] shown in Fig. 3(d) signifies a noisy and broad structure, while the stable pulsation SM [Fig. 3(e)] in Fig. 3(c) suggests a neat pulsation frequency with narrow linewidth and high SNR, demonstrating the different stability properties of the pulsation frequency for the two SM states. The RF spectrum of SMs with stationary operation and pulsation frequency locking measured through the radio spectrum analyzer can be found in Fig. S7 in the Supplementary Material.

In addition to the high stability and periodicity of pulsation SMs, it is also able to achieve intelligent control of other parameters of pulsation SMs in the laser, e.g., the pulsation ratio. Here, the pulsation ratio is defined as the ratio of the largest to the lowest amplitude of the pulse spectrum in a pulsation period. The pulsation ratio is proportional to the strength of the sideband in the RF spectrum; thereby, we can optimize the desired pulsation ratio by considering the strength of the RF sideband in the defined merit function. By utilizing the GA and slightly modifying the fitness function (see Appendix), the SM with tunable pulsation ratio can be generated. Figure 4 shows the DFT spectra and field autocorrelation trace of three examples of doublet SMs with different pulsation ratios that were generated in the laser at a pump power of 420 mW. Figures 4(a) and 4(b) exhibit the weakest pulsation regime of SMs, and the moderate and strongest pulsation operations of SMs are shown in Figs. 4(d), 4(e), 4(g), and 4(h), respectively. The single-shot spectra of the maximal and minimal spectrum extents within a pulsation period [Figs. 4(c), 4(f), and 4(i)] reveal the major difference in the pulsation ratio among three types of doublet SMs. The significant peak-to-dip flip in the spectrum [Fig. 4(i)]

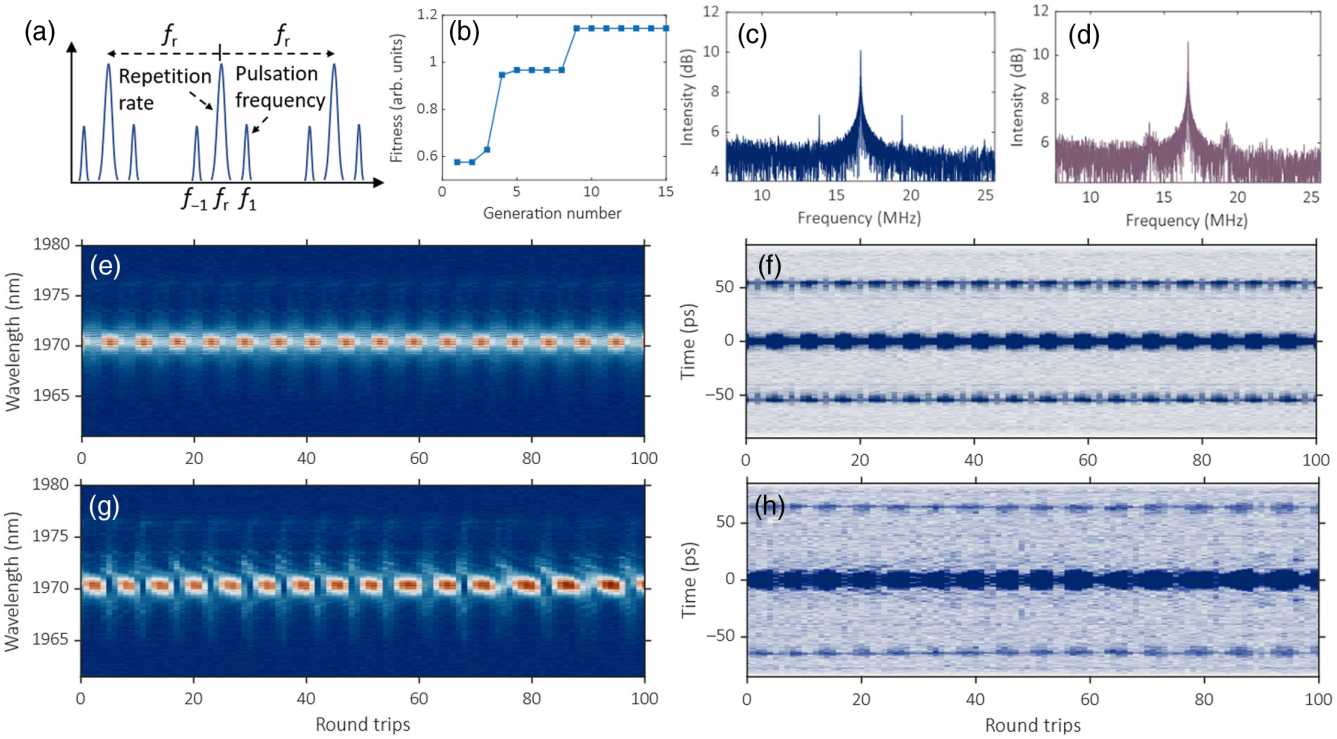

Fig. 3 Pulsation SM with and without EA optimization. (a) Sketch of the RF signal under pulsation SM operation, where f_r is the cavity repetition rate and the sideband frequency $f_{\pm 1}$ is a manifestation of SMs with pulsation frequency $|f_{\pm 1} - f_r|$. (b) Evolution of the best merit score over successive generations. RF spectra of SM in (c) with pulsation frequency locking correspond to a single-mode oscillation and in (d) without pulsation frequency locking correspond to unstable multimode oscillation. (e) DFT spectra and (f) field autocorrelation trace evolution of frequency-locked pulsation SM showing a well-defined periodicity. (g) DFT spectra and (h) field autocorrelation trace evolution of frequency-unlocked pulsation SM showing a degraded periodicity.

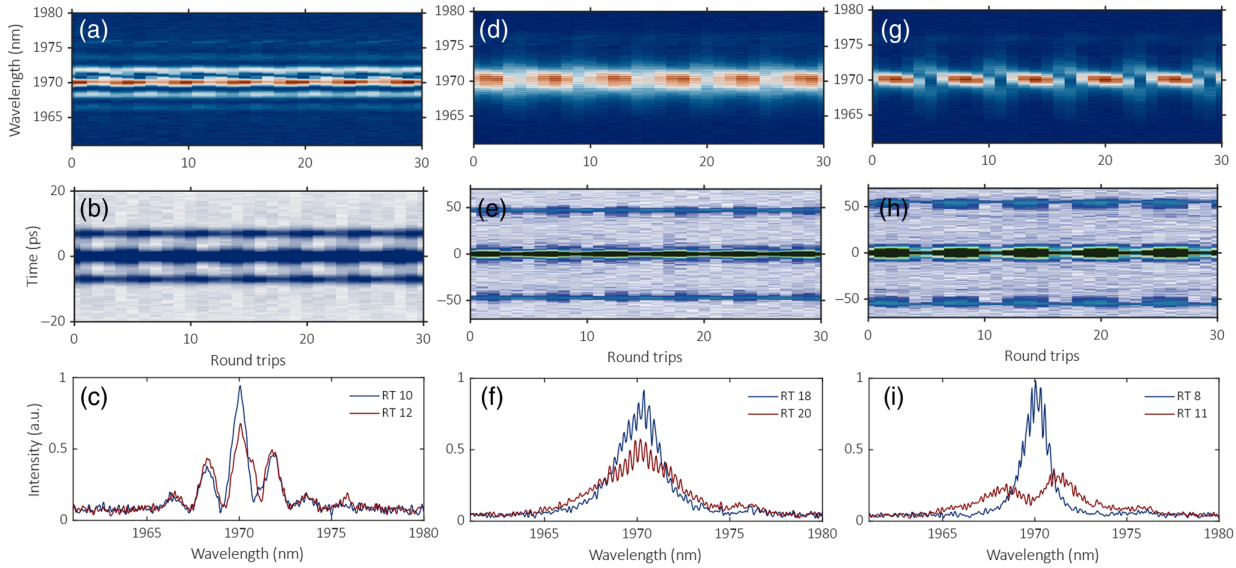

Fig. 4 Evolutionary algorithm optimization results for doublet SMs with a tunable pulsation ratio. Dynamics of doublet SMs with (a)–(c) small, (d)–(f) moderate, and (g)–(i) large pulsation ratios. (a), (d), and (g) DFT spectral evolution over consecutive cavity RTs. (b), (e), and (h) Field autocorrelation trace evolution over consecutive cavity RTs. (c), (f), and (i) Single-shot spectra of maximal and minimal spectrum extents within a pulsation period.

demonstrates the stronger pulsation ratio, resembling the spectral variation in period-doubling bifurcation.[49] In contrast, the amplitude of the spectral interference fringe in Fig. 4(c) has a smaller change, verifying the weak pulsation operation. In addition, a good agreement between the spectra measured by OSA and the single-shot DFT spectrum of large and small pulsation ratios can be found in Fig. S8 in the Supplementary Material.

Further, the $(2+2)$ SMCs, bounded by two soliton pair molecules with nanosecond intermolecular temporal separation, can be generated in the fiber laser by slightly increasing the pump power to 460 mW. Similarly, using EA and modified fitness function, a $(2+2)$ SMC with a tunable pulsation ratio can be achieved. The DFT spectra and field autocorrelation trace evolution in Fig. 5 exhibit the three examples of $(2+2)$

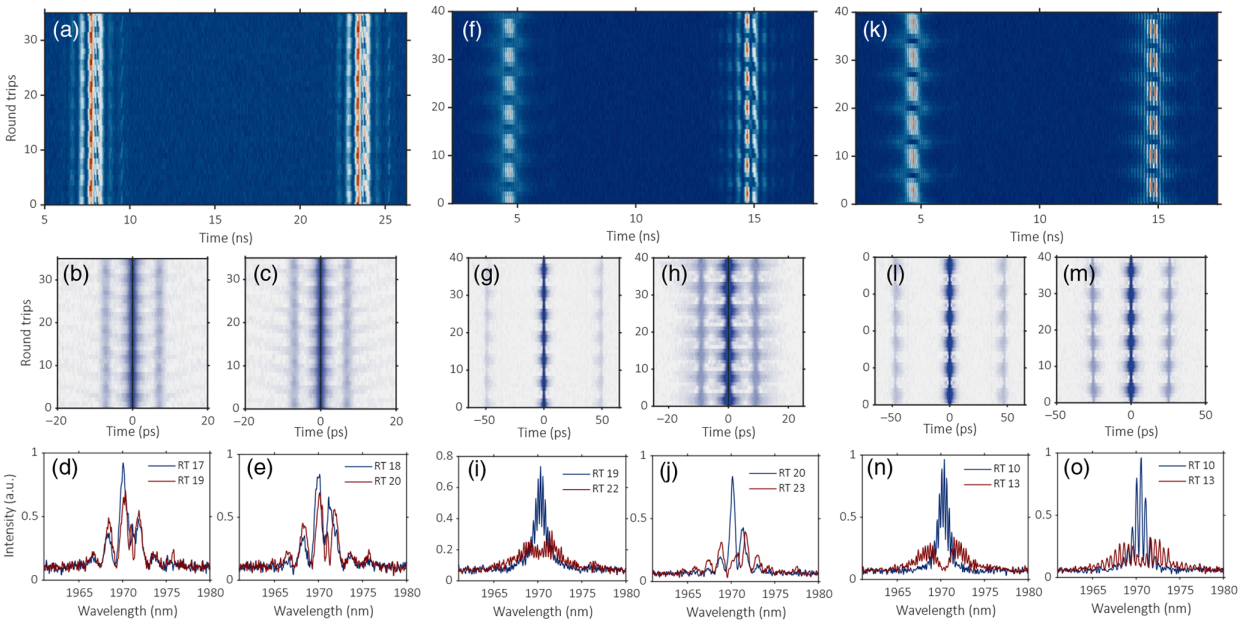

Fig. 5 Evolutionary algorithm optimization results for $(2+2)$ SMCs with a tunable pulsation ratio. Dynamics of $(2+2)$ SMC with (a)–(e) small, (f)–(j) moderate, and (k)–(o) large pulsation ratio. (a), (f), (k) DFT spectral evolution over consecutive cavity RTs. (b), (c), (g), (h), (l), and (m) Field autocorrelation trace evolution over consecutive cavity RTs. (d), (e), (i), (j), (n), and (o) Single-shot spectra of maximal and minimal spectrum extents within a pulsation period.

SMCs with different pulsation ratios. The weakest pulsation operation of an SMC is shown in Figs. 5(a)–5(e), and the moderate and strongest pulsation ratios of an SMC are shown in Figs. 5(f)–5(o), respectively. The discrepancy in the pulsation ratio of the three types of SMCs can be further resolved in the single-shot spectra of maximal and minimal spectrum extents within a pulsation period. The peak-to-dip flip in spectra can also be observed in SMC with the strongest pulsation ratio [Figs. 5(n) and 5(o)]. The different spectral modulation periods indicate the different intersoliton temporal separations of the leading and trailing soliton pair molecule, which is consistent with the field autocorrelation trace evolution [Figs. 5(l) and 5(m)]. Similarly, the central amplitude of the spectra in the SMC also exhibits significant variation in Figs. 5(i) and 5(j), verifying the moderate pulsation ratio. The leading soliton pair molecule has a different spectral shape and larger intersoliton temporal interval compared to the trailing part [Figs. 5(g) and 5(h)]. In contrast, the spectral variation of the SMC in a pulsation period is small in Figs. 5(d) and 5(e), demonstrating the weakest pulsation operation. For this case, the leading and trailing soliton pair molecules have the same spectral shape and intersoliton separation [Figs. 5(b) and 5(c)]. Notably, the leading and trailing soliton pair molecules in the SMC have the same pulsation period in the three examples, while the leading SM has a lag synchronization of ∼1 RT compared to the trailing part in the weakest and moderate pulsation ratio [Figs. 5(d), 5(e), 5(i), and 5(j)]. And the good synchronization of the leading and trailing SMs can be resolved in the SMC with the strongest pulsation ratio [Figs. 5(n) and 5(o)].

In addition to the parameter of pulsation ratio, pulsation period is another important parameter of the SM that can be controlled in the laser. In this experiment, the pulsation period of the SM mainly concentrated on 5 or 6 RT, which obviously restricted the search regime of the EA. This also demonstrates that net cavity dispersion plays a crucial role in the variation range of SM pulsation periods, except for the gain/loss and nonlinearity that can be altered through EPC. The DFT spectra and field autocorrelation trace evolution of triplet pulsation SM and $(2+1)$ SMC with tunable pulsation ratio can be found in Figs. S9 and S10 in the Supplementary Material.

2.4 Controllable SM Switching and Encoding

Benefiting from the reliable and efficient EA-based optimization approach, we further explored the controllable multiswitching of SMs with different states in the laser by changing the optimized driving voltage of the EPC. The SM properties (pulsation or stationary operation, different intersoliton temporal separations) are mostly determined by spectra features. Here, we first search two stationary SM states with different intersoliton separations through an EA and record the optimized drive voltage of the EPC. The desired spectral pattern and NMSE serve as the fitness function. Then the controllable continuous switching of two stationary SMs can be achieved by simply altering the drive voltage of the EPC. The corresponding DFT spectra and field autocorrelation trace are shown in Figs. 6(a) and 6(d), exhibiting the different spectral modulation periods and distinct intersoliton separation. The high fidelity can be resolved during this continuous switching, verifying the repeatability and reliability of the EA. Similarly, the controllable continuous switching between pulsation and stationary SMs can also be achieved by changing the optimized drive voltage of each state. The DFT spectra and field autocorrelation trace evolution are shown in Figs. 6(c) and 6(d). The stationary SM has obviously different spectral characteristics and larger intersoliton separation compared to the pulsation state.

In addition to the continuous switching between two states, the multistate switching of SMs can also be realized by alternating the drive voltage of the EPC. The controllable continuous switching of SMs among three different states can be observed. The corresponding DFT spectra- and field-autocorrelated trace evolution are shown in Figs. 6(e) and 6(f). During one switching period, the pulsation SM first transitions to a stationary state with a larger soliton temporal interval, subsequently switching to another stationary state with a larger spectral modulation period and a decrease in intersoliton temporal separation. Similarly, continuous switching of SMs among four different states can be achieved by varying four optimized drive voltages, as shown in Figs. 6(g) and 6(h). Four different SM states can be clearly identified in one switching period with different spectral features, including two pulsation states with different pulsation ratios and two stationary states with distinct intersoliton separation.

Akin to the doublet SM, the controllable continuous switching of a triplet SM can be realized by changing the drive voltage of the EPC at the pump power of 440 mW. Figures 6(i)–6(l) depict the DFT spectra and field autocorrelation trace evolution, indicating two types of continuous switching of stationary triplet SMs between two states with different intersoliton temporal separations. The optical spectrum and internal motions of each doublet and triplet SM state during continuous switching can be found in Figs. S11 and S12 in the Supplementary Material. Apart from this, the reproducibility and stability of SMs with the application of the EPC can be found in Figs. S13 and S14 in the Supplementary Material.

The controllable deterministic switching of SMs with different operation states in a single fiber laser is beneficial for extended applications in optical computing, information encoding, and soliton communication.[29] As a proof of concept, we conduct the quaternary digital encoding using four doublet SM states with different spectral features: the SMs with weak ("3") and moderate pulsation ratio ("1") and stationary SMs with small ("0") and large ("2") intersoliton temporal separation [Fig. 6(g)]. The conversion of multiple SM states can be achieved by altering the drive voltage of the EPC. As a result, the optical quaternary codes of HKU (1020|1023|1111, an abbreviation of the University of Hong Kong) and ABIC (1001|1002|1021|1003, an abbreviation of the Advanced Biomedical Instrumentation Centre) can be obtained by programming the drive voltage, as shown in Fig. 7. Each letter can be encoded by 4 bits with a total of 120 consecutive cavity RTs. In this experiment, the maximum switching frequency that can be achieved is ∼10 Hz, which is mainly restricted by the refresh rate of the EPC. Analysis with DFT spectral evolution of the doublet SM in Fig. 2(g) shows the time interval between the two states' switching is ∼70 μs. Thereby, it can be expected that the SMs multistate switching frequency can be scaled to kilohertz by introducing a faster polarization adjustment device. This multiletter test further verifies the availability of SM-based digital encoding in this platform beyond the conventional telecom band and offers new prospects in ultrafast laser applications.

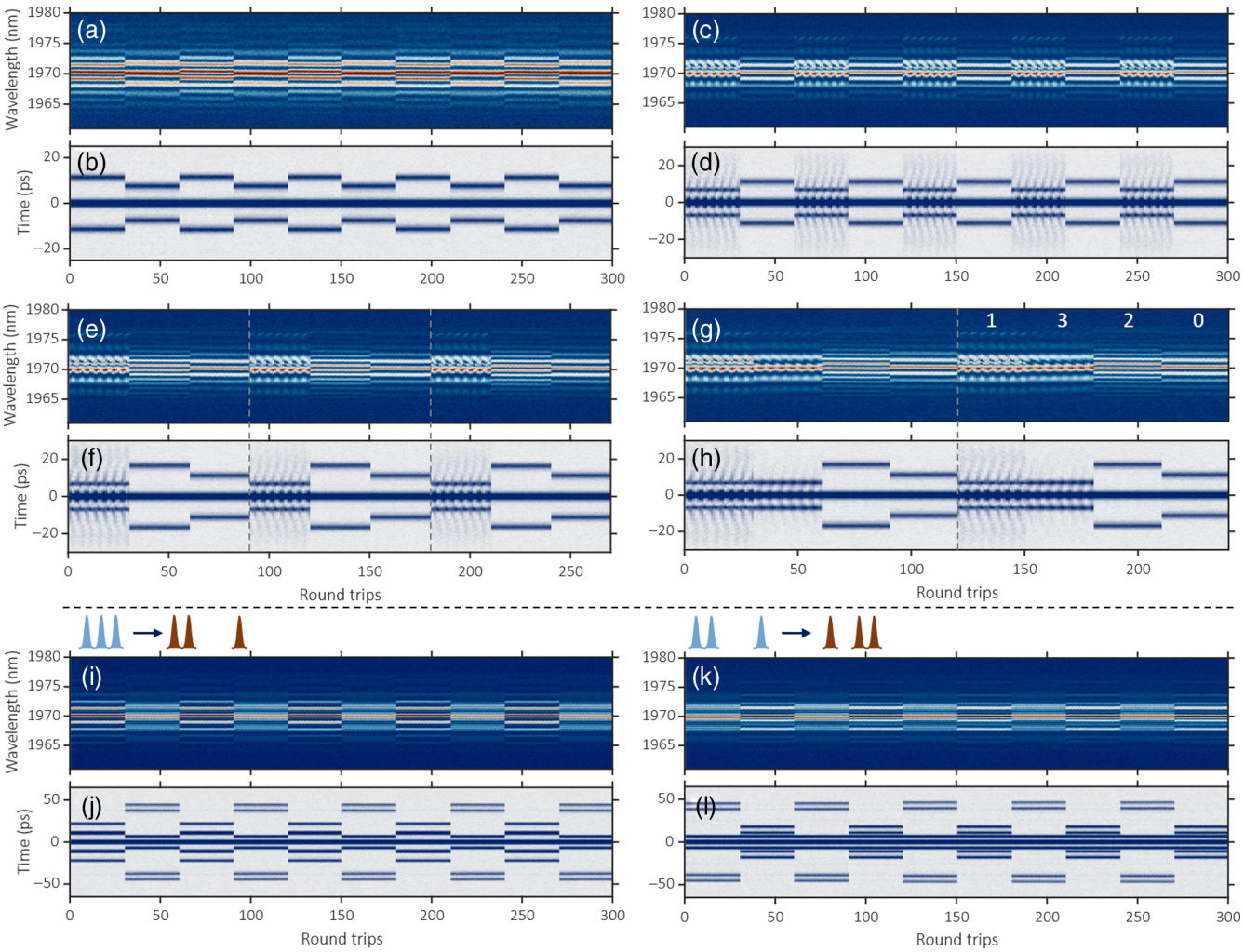

Fig. 6 Controllable continuous switching of doublet and triplet SMs. (a)–(h) Controllable switching of doublet SM. (a), (b) Continuous switching of stationary SM with different temporal separations. (c), (d) Continuous switching of SM between pulsation and stationary states. (e), (f) Continuous switching of SM among three states. (g), (h) Continuous switching of SM among four states. (i)–(j) Controllable switching of triplet SM. (k)–(l) Continuous switching of SM between two states with different temporal separations. (a), (c), (e), (g), (i), and (k) DFT spectral evolution over consecutive cavity RTs. (b), (d), (f), (h), (j), and (l) Field autocorrelation trace evolution over consecutive cavity RTs.

3 Conclusion

We have demonstrated, for the first time to our knowledge, the intelligent control of SMs in an NPR-based 2 μm ultrafast fiber laser enabled by a dedicated design EA, simultaneously opening an emerging window toward longer wavelengths. With the high-precision feedback loop, the spectral shape programming of SMs corresponding to versatile operation states can be achieved, involving stationary or pulsation states in doublet and triplet SMs and different intersoliton temporal separations characterized by a specific spectral modulation period. Benefiting from the reliable and efficient EA-based optimization approach, the controllable continuous switching of SMs with different states can be realized by altering the optimized drive voltage of the EPC. With a modified merit function that is derived from the features of the RF spectrum, the high-stability pulsation SM along with frequency locking can be achieved, which is attractive for high-resolution spectroscopy applications. The doublet and SMCs with controllable pulsation ratios can also be accessed under a user-defined fitness function to tailor the parameters of pulsation SMs. Further, digital quaternary encoding was demonstrated in this platform by employing the self-assembled characteristics of SMs, which may stimulate advanced applications of coherent optical communications, all-optical storage, and optical computations.

Compared to the automatic generation of SMs during the transient or nonequilibrium evolution, our work concentrated on exploring SMs with high stability and reproducibility with the application of an EPC. The SM generally experiences pulse shaping in the laser, which is mainly influenced by the balance between dispersion/nonlinearity and gain/loss. The control over the number of solitons and fine variation of soliton energy and duration within the specified mode-locked regime can be achieved by tuning the pump power.[50] Meanwhile, the broad

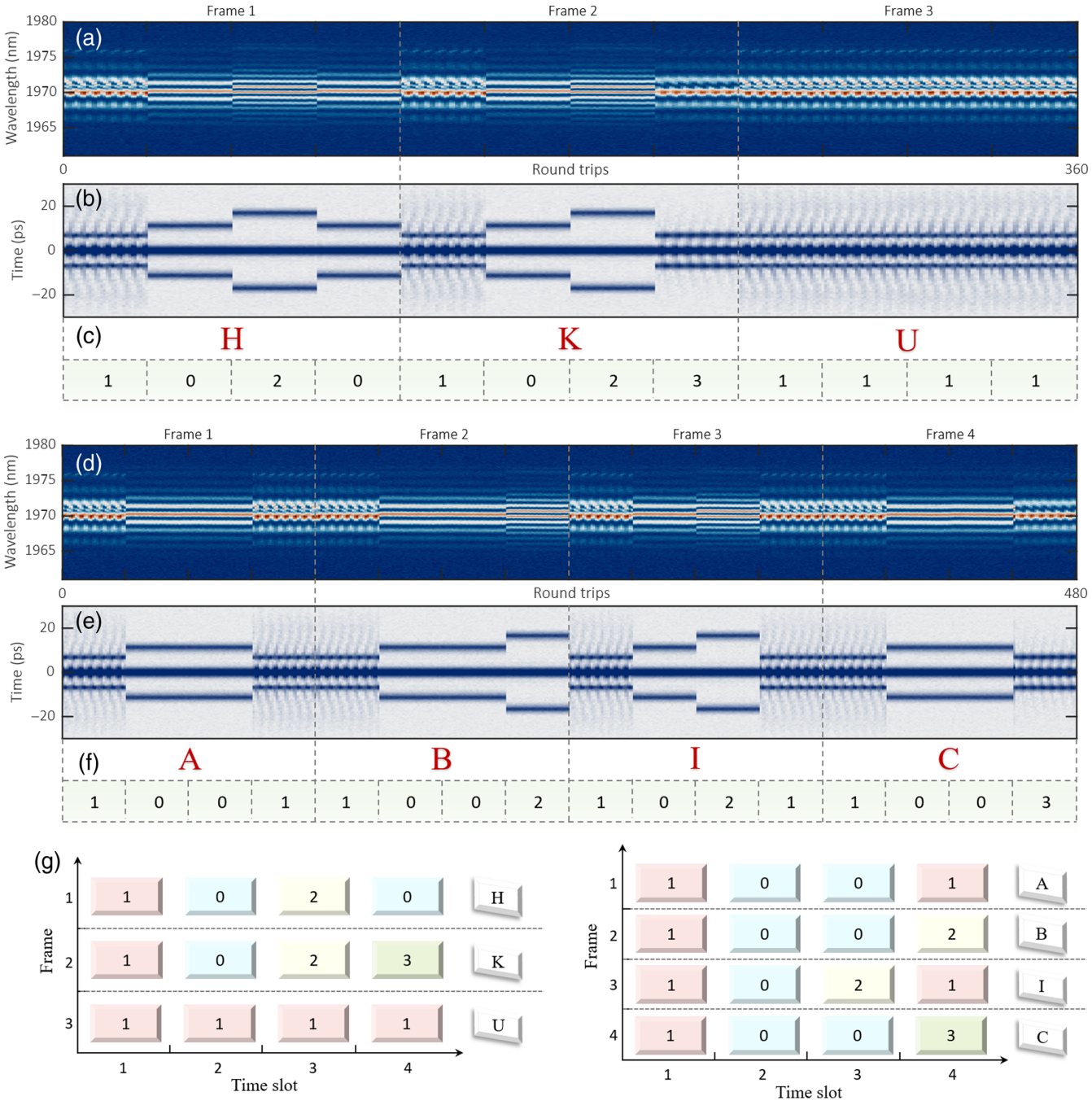

Fig. 7 Exemplary multiletter encoding based on the doublet SM of four assembled forms. (a), (d) Successive recording of the encoded DFT streams. The pump power is set at 420 mW, and the EPC is modulated by four different drive voltages. (b), (e) Field autocorrelation trace evolution. (c), (f) ASCII quaternary format codes for each letter, which contain four bits. (g) Visualization of each letter. Each frame is composed of four time slots and represents a single letter.

variation of SM parameters can also be observed in the NPR-based mode-locked laser by varying intracavity polarization, corresponding to altering the nonlinear transfer function in the laser that exits plentiful parameter space. Further, the evolutionary algorithm can significantly facilitate the search for the optimized state of SMs. For instance, the drive voltage range of pulsation frequency locking of SMs in this work is quite narrow, at ~0.2 V, compared to the whole tuning range of 100 V of the EPC. Combining the EPC and EAs can quickly converge the SM to the desired state, thus generating an SM with the desired properties of more efficiency and high reproducibility. Although the EA presented here is used for the 2 μm mode-locked fiber laser, the tailored merit function may also inspire the exploration of plentiful dissipative soliton dynamics on other nonlinear systems, such as ultrafast fiber lasers operated in visible or mid-infrared wavelengths, microresonators, and fiber Kerr resonators.

We believe the elegant and intelligent control of SMs presented in this work can find novel applications in laser optics and can hold potential for new possibilities in optical information domains.

4 Appendix: Methods

4.1 Evolution Algorithm

The search algorithm in this experiment is based on the modified GA, which focuses on regulating the polarization state in the laser by optimizing the drive voltage of the EPC. First, for the spectral shape programming to determine the different SM states, the fitness is the NMSE between the current and standard spectral shapes. The objective spectra can be successfully acquired when the NMSE between the current pulse and standard pulse is lower than a preset threshold.

Subsequently, for the pulsation SM generation with high stability and pulsation frequency locking, we defined the following merit function for the autosetting of an optimized pulsation regime:

$$F_{\text{merit}} = \alpha \times C_{\text{ml}} + \beta \times C_p. \tag{1}$$

Among them, the weights of α and β are defined empirically. C_{ml} corresponds to the merit function associated with the mode-locking state of the laser,

$$C_{\text{ml}} = \sum_{i=1}^{i=N} I_i/N, I_i = \begin{cases} I_i, & (I_i \geq I_{\text{th}}) \\ 0, & (I_i < I_{\text{th}}) \end{cases}, \tag{2}$$

where N is the number of laser output intensity points recorded by the oscilloscope, I_i is the intensity at point i, and I_{th} is the intensity threshold higher than the noise. Therefore, C_{ml} is the average intensity of pulses to exclude laser instability regimes, such as relaxation oscillation. The second term C_p in the merit function is utilized to differentiate between stationary and pulsation regimes and simultaneously maintain a pulsation frequency-locked mode,

$$C_p = (\max I_1(f_+) + \max I_{-1}(f_-))/\gamma, \begin{matrix} f_+ \in [f_1 - \Delta, f_1 + \Delta] \\ f_- \in [f_{-1} - \Delta, f_{-1} + \Delta] \end{matrix}, \quad \Delta < f_r/2. \tag{3}$$

The feature of the pulsation frequency emerges as two symmetrical sidebands $f_{\pm 1}$ around the cavity repetition frequency f_r. There are no sidebands when the SMs operate at a stationary state, and the intensity of the sideband ($f_{\pm 1}$) is related to the pulsation ratio of the SMs. The maximum sideband intensity ($f_{\pm 1}$) plays a vital role in distinguishing the general pulsation SM and the high-stability SM along with the pulsation frequency-locked mode.

Further, the key to tuning the pulsation ratio of SMs is to control the sideband frequency intensity of the laser output; the defined merit function is shown as

$$F_{\text{pr}} = \alpha \times C_{\text{ml}} + \beta \times (C_{\text{const}} - |C_p - C_{\text{set}}|). \tag{4}$$

C_{const} represents a constant and the higher C_p value corresponds to a larger pulsation ratio. $|C_p - C_{\text{set}}|$ is proportional to the difference between the measured pulsation ratio and the target value (C_{set}). Therefore, the merit score increases as the pulsation ratio of the SM approaches the target value. During optimization, the RF spectrum is calculated through a fast Fourier transform of the laser intensity recorded by the oscilloscope.

4.2 Numerical Simulation

To confirm and elucidate the mechanism of the SMs switching between different states, numerical simulations are executed in a lumped propagation model. The propagation of solitons within the fiber section is modeled with a nonlinear Schrödinger equation, which takes the following form:

$$\frac{\partial u(z,t)}{\partial z} = -i\frac{\beta_2}{2}\frac{\partial^2 u(z,t)}{\partial t^2} + \frac{g}{2\Omega_g^2}\frac{\partial^2 u(z,t)}{\partial t^2} + i\gamma|u(z,t)|^2 u(z,t) + \frac{g}{2}u(z,t), \tag{5}$$

where u is the slowly varying envelope moving at the group velocity along the propagation coordinate z, β_2 and γ are the second-order dispersion coefficients and Kerr nonlinearity, respectively, and Ω_g is the gain bandwidth. The gain is described by $g = g_0 \exp(-E_p/E_s)$, where g_0 is the small signal gain, which is nonzero only in the gain fiber, E_p is the pulse energy, and E_s is the gain saturation energy determined by pump power.

The nonlinear transfer function of the saturable absorber is modeled by

$$T = R_0 + \Delta R[1 - 1/(1 + P/P_0)], \tag{6}$$

where R_0 is the unsaturated reflectance, ΔR is the saturable reflectance, P is the pulse instantaneous power, and P_0 is the saturation power. The numerical model is solved with a standard symmetric split-step propagation algorithm, and the parameters used in the simulation follow typical experimental values.

Disclosures

The authors declare no competing interests.

Code and Data Availability

Data underlying the results presented in this paper may be obtained from the authors upon reasonable request.

Acknowledgments

This work was supported by the Research Grants Council of the Hong Kong Special Administrative Region of China (Grant Nos. HKU 17212824, HKU 17210522, HKU C7074-21G, HKU R7003-21, and HKU 17205321), the Innovation and Technology Commission of the Hong Kong SAR Government (Grant Nos. MHP/073/20 and MHP/057/21), and the Health@InnoHK program.

References

1. C. Kerse et al., "Ablation-cooled material removal with ultrafast bursts of pulses," *Nature* **537**, 84–88 (2016).
2. D. Z. Tan, B. Zhang, and J. R. Qiu, "Ultrafast laser direct writing in glass: thermal accumulation engineering and applications," *Laser Photonics Rev.* **15**, 2000455 (2021).
3. H. D. A. Santos et al., "Ultrafast photochemistry produces superbright shortwave infrared dots for low-dose in vivo imaging," *Nat. Commun.* **11**, 2933 (2020).

4. E. E. Hoover and J. A. Squier, "Advances in multiphoton microscopy technology," *Nat. Photonics* **7**, 93–101 (2013).
5. S. R. Leone and D. M. Neumark, "Probing matter with nonlinear spectroscopy," *Science* **379**, 536–537 (2023).
6. M. Pang et al., "All-optical bit storage in a fibre laser by optomechanically bound states of solitons," *Nat. Photonics* **10**, 454–458 (2016).
7. G. Herink et al., "Real-time spectral interferometry probes the internal dynamics of femtosecond soliton molecules," *Science* **356**, 50–54 (2017).
8. S. T. Cundiff, J. M. Soto-Crespo, and N. Akhmediev, "Experimental evidence for soliton explosions," *Phys. Rev. Lett.* **88**, 073903 (2002).
9. A. F. J. Runge, N. G. R. Broderick, and M. Erkintalo, "Observation of soliton explosions in a passively mode-locked fiber laser," *Optica* **2**, 36–39 (2015).
10. J. Peng et al., "Breathing dissipative solitons in mode-locked fiber lasers," *Sci. Adv.* **5**, eaax1110 (2019).
11. Y. Zhou et al., "Breathing dissipative soliton explosions in a bidirectional ultrafast fiber laser," *Photonics Res.* **8**, 1566–1572 (2020).
12. D. R. Solli et al., "Optical rogue waves," *Nature* **450**, 1054–1057 (2007).
13. Y. Zhou et al., "Unveiling laser radiation of multiple optical solitons by nonlinear Fourier transform," *Laser Photonics Rev.* **17**, 2200731 (2023).
14. P. Grelu and N. Akhmediev, "Dissipative solitons for mode-locked lasers," *Nat. Photonics* **6**, 84–92 (2012).
15. P. Grelu, "Solitary waves in ultrafast fiber lasers: from solitons to dissipative solitons," *Opt. Commun.* **552**, 130035 (2024).
16. W. B. He et al., "Synthesis and dissociation of soliton molecules in parallel optical-soliton reactors," *Light Sci. Appl.* **10**, 120 (2021).
17. K. Krupa et al., "Real-time observation of internal motion within ultrafast dissipative optical soliton molecules," *Phys. Rev. Lett.* **118**, 243901 (2017).
18. A. Zavyalov et al., "Dissipative soliton molecules with independently evolving or flipping phases in mode-locked fiber lasers," *Phys. Rev. A* **80**, 043829 (2009).
19. J. S. Peng et al., "Breather molecular complexes in a passively mode-locked fiber laser," *Laser Photonics Rev.* **15**, 2000132 (2021).
20. Y. Zhou et al., "Buildup and dissociation dynamics of dissipative optical soliton molecules," *Optica* **7**, 965–972 (2020).
21. S. Hamdi et al., "Superlocalization reveals long-range synchronization of vibrating soliton molecules," *Phys. Rev. Lett.* **128**, 213902 (2022).
22. Z. Q. Wang et al., "Optical soliton molecular complexes in a passively mode-locked fibre laser," *Nat. Commun.* **10**, 830 (2019).
23. J. M. Soto-Crespo, G. N. Akhmediev, and N. Devine, "Soliton complexes in dissipative systems: vibrating, shaking, and mixed soliton pairs," *Phys. Rev. E* **75**, 016613 (2007).
24. Y. Zhou et al., "Reconfigurable dynamics of optical soliton molecular complexes in an ultrafast thulium fiber laser," *Commun. Phys.* **5**, 1–11 (2022).
25. W. He et al., "Formation of optical supramolecular structures in a fibre laser by tailoring long-range soliton interactions," *Nat. Commun.* **10**, 5756 (2019).
26. K. Goda and B. Jalali, "Dispersive Fourier transformation for fast continuous single shot measurements," *Nat. Photonics* **7**, 102–112 (2013).
27. F. Kurtz, C. Ropers, and G. Herink, "Resonant excitation and all-optical switching of femtosecond soliton molecules," *Nat. Photonics* **14**, 9–13 (2020).
28. L. Nimmesgern et al., "Soliton molecules in femtosecond fiber lasers: universal binding mechanism and direct electronic control," *Optica* **8**, 1334–1339 (2021).
29. Y. Liu et al., "Phase-tailored assembly and encoding of dissipative soliton molecules," *Light Sci. Appl.* **12**, 123 (2023).
30. Y. Zhou et al., "Breathing dissipative soliton molecule switching in a bidirectional mode-locked fiber laser," *Adv. Photonics Res.* **3**, 2100318 (2022).
31. Y. Yang et al., "Phase-encoding of loosely bound soliton molecules," *APL Photonics* **9**, 031305 (2024).
32. S. L. Liu et al., "On-demand harnessing of photonic soliton molecules," *Optica* **9**, 240–250 (2022).
33. U. Andral et al., "Fiber laser mode locked through an evolutionary algorithm," *Optica* **2**, 275–278 (2015).
34. U. Andral et al., "Toward an autosetting mode-locked fiber laser cavity," *J. Opt. Soc. Am. B* **33**, 825–833 (2016).
35. R. I. Woodward and E. J. R. Kelleher, "Genetic algorithm-based control of birefringent filtering for self-tuning, self-pulsing fiber lasers," *Opt. Lett.* **42**, 2952–2955 (2017).
36. G. Pu et al., "Intelligent programmable mode-locked fiber laser with a human-like algorithm," *Optica* **6**, 362–369 (2019).
37. X. Wei et al., "Harnessing a multi-dimensional fibre laser using genetic wavefront shaping," *Light Sci. Appl.* **9**, 149 (2020).
38. G. Genty et al., "Machine learning and applications in ultrafast photonics," *Nat. Photonics* **15**, 91–101 (2021).
39. G. Pu et al., "Intelligent control of mode-locked femtosecond pulses by time-stretch-assisted real-time spectral analysis," *Light Sci. Appl.* **9**, 13 (2020).
40. X. Wu et al., "Intelligent breathing soliton generation in ultrafast fiber lasers," *Laser Photonics Rev.* **16**, 2100191 (2022).
41. X. Wu et al., "Farey tree and devil's staircase of frequency-locked breathers in ultrafast lasers," *Nat. Commun.* **13**, 5784 (2022).
42. H. Liang et al., "Optimum spectral window for imaging of art with optical coherence tomography," *Appl. Phys. B* **111**, 589–602 (2013).
43. C. Xu and F. Wise, "Recent advances in fibre lasers for nonlinear microscopy," *Nat. Photonics* **7**, 875–882 (2013).
44. D. Kong et al., "Super-broadband on-chip continuous spectral translation unlocking coherent optical communications beyond conventional telecom bands," *Nat. Commun.* **13**, 4139 (2022).
45. K. Zou et al., "High-capacity free-space optical communications using wavelength-and mode-division-multiplexing in the mid-infrared region," *Nat. Commun.* **13**, 7662 (2022).
46. K. K. Tsia et al., "Performance of serial time-encoded amplified microscope," *Opt. Express* **18**, 10016–10028 (2010).
47. T. Xian et al., "Subharmonic entrainment breather solitons in ultrafast lasers," *Phys. Rev. Lett.* **125**, 163901 (2020).
48. X. Wu et al., "Synchronization, desynchronization, and intermediate regime of breathing solitons and soliton molecules in a laser cavity," *Phys. Rev. Lett.* **131**, 263802 (2023).
49. Z. Q. Wang et al., "Spectral pulsations of dissipative solitons in ultrafast fiber lasers: period doubling and beyond," *Laser Photonics Rev.* **17**, 2200298 (2023).
50. A. Kokhanovskiy, E. Kuprikov, and S. Kobtsev, "Single-and multi-soliton generation in figure-eight mode-locked fibre laser with two active media," *Opt. Laser Technol.* **131**, 106422 (2020).

Biographies of the authors are not available.